arXiv:nucl-th/9908060v3 7 Sep 1999

High-spin yrast structure of ^{32}S suggested by symmetry-unrestricted, cranked Hartree-Fock calculations

Masayuki Yamagami and Kenichi Matsuyanagi
Department of Physics, Graduate School of Science,
Kyoto University, *Kitashirakawa, Kyoto 606-8502, Japan*

19 August 1999

Abstract

High-spin yrast structure of ^{32}S is investigated by means of the cranked Skyrme-Hartree-Fock method in the three-dimensional Cartesian-mesh representation without imposing restrictions on spatial symmetries. The result suggests that 1) a crossover from the superdeformed to the hyperdeformed-like configurations takes place on the yrast line at angular momentum $I \simeq 24$, which corresponds to the "band termination" point in the cranked harmonic-oscillator model, and 2) non-axial octupole deformations of the Y_{31} type play an important role in the yrast states in the range $5 \leq I \leq 13$.

PACS: 21.60-n; 21.60.Jz; 27.30.+t
Keywords: Cranked Skyrme-Hartree-Fock method; Superdeformation; Non-axial octupole deformation; Yrast line; High-spin state; Sulfur 32

1 Introduction

Since the discovery of the superdeformed(SD) rotational band in ^{152}Dy, about two hundreds SD bands have been found in various mass (A=60, 80, 130, 150, 190) regions [1–6]. It turned out that every regions of superdeformation have their own characteristics and offer a number of interesting questions; investigations of them have been significantly enlarging and deepening our understanding of nuclear structure. Yet, the doubly magic SD band in ^{32}S, which has been expected quite a long time [7–10] remains unexplored, and will become a great challenge in the coming years [6]. Exploration of the SD band in ^{32}S will certainly give a strong impact toward understanding the possible connection between the SD structure and the molecular resonance phenomena associated with the ^{16}O $+^{16}$O configurations (see, e.g. [11, 12] for reviews). More generally speaking, the nucleus ^{32}S seems to be situated in a key position in the investigation of possible relationships (such as discussed in [13–15]) between the SD states systematically observed in heavy nuclei and the cluster structures widely observed in light nuclei (see, e.g. [16] for a review). Thus, excited states in ^{32}S have been theoretically studied by Nilsson-Strutinsky approaches [7–10], selfconsistent mean-field approaches [17,18], spherical shell-models [19, 20], and cluster-structure and molecular-resonance points of view [21–25].

The aim of this paper is to study the high-spin yrast structure of ^{32}S from the point of view of exploring exotic shapes in nuclear high-spin states by means of the cranked Hartree-Fock (HF) method with the use of the Skyrme forces [26, 27], which is called "the cranked SHF method". One of the recent advances in nuclear structure theory is that it has become possible to carry out the HF calculation in the three-dimensional (3D) Cartesian-mesh representation [28–30, 32]. This approach has been extended [18, 33, 34] to a rotating frame by introducing the cranking term and applied to the high-spin yrast states of ^{32}S in Ref. [18] with the use of the BKN interaction [31]. In these cranked HF calculations, however, parity and signature symmetries are assumed for the intrinsic wave functions in order to simplify the calculation. We refer an excellent review by Åberg, Flocard and Nazarewicz [2] for an overview of studies on nuclear shapes in terms of various kinds of mean-field theory, especially other than the cranked SHF approach.

Recently, we constructed a new computer code for the cranked SHF calculation based on the 3D Cartesian-mesh representation, which provides a powerful tool for exploring exotic shapes (breaking both axial and reflection symmetries in the intrinsic states) at high spin in unstable nuclei as well as in stable nuclei. As a first application of this new code, we investigated the high-spin yrast structure of ^{32}S, and found [35] that 1) a drastic structure change may occur above angular momentum $I \simeq 24$ in the yrast line, and 2) non-axial octupole deformations of the Y_{31} type arise in the yrast line in the range $5 \leq I \leq 13$. The present paper is intended to give a more detailed account of this work. Quite recently, Molique, Dobaczewski and Dudek [36] investigated

several SD configurations in ^{32}S (not restricted to the yrast states) as well as in neighboring odd-A nuclei by means of the cranked SHF method with the SLy4 force [37] in the harmonic oscillator basis. On the other hand, they did not discuss the yrast states above $I \simeq 24$ as well as non-axial octupole deformations, which are the major subjects of this paper.

After a brief account of the cranked SHF calculational method in Section 2, an overview of the obtained yrast line for ^{32}S is given in Section 3. In Section 4, we discuss properties of the high-spin limit of the SD band, paying special attention to a band-crossing phenomenon associated with the level crossing with the rotation-aligned $[440]\frac{1}{2}$ level. The result of the cranked SHF calculation is compared in Section 5 with that of the cranked harmonic oscillator (CHO) model calculation. In Section 6, effects of the rotation-induced, time-odd components in the selfconsistent mean field on the properties of the SD band are briefly discussed. In Section 7, we discuss about the Y_{31} deformed solutions of the cranked SHF equations, which constitute the yrast line in the range $5 \leq I \leq 13$. Although, at the present time, experimental data directly comparable with our theoretical calculations seem to be unavailable, we briefly remark in Section 8 on some recent experimental references. Conclusion is given in Section 9.

2 Cranked SHF calculation

The cranked HF equation for a system uniformly rotating about the x-axis is given by

$$\delta < H - \omega_{\rm rot} J_x >= 0, \tag{1}$$

where $\omega_{\rm rot}$ and J_x mean the rotational frequency and the x-component of angular momentum, and the bracket denotes the expectation value with respect to a Slater determinantal state. We solve the cranked HF equation for a Hamiltonian of the Skyrme type by means of the imaginary-time evolution technique [28] in the 3D Cartesian-mesh representation. We adopt the standard algorithm [28–30,34] in the numerical calculation, but completely remove various restrictions on spatial symmetries. Namely, we basically use the procedure developed and applied to the yrast line of ^{24}Mg by Bonche, Flocard and Heenen [34], except that the parity and the signature symmetries are not imposed on the individual wave functions. In this connection, we mention that a similar HF code (with parity projection but without the cranking term) was constructed by Takami et al. [38] and successfully applied to the description of cluster structures in light nuclei, ^{8}Be, ^{12}C, ^{16}O and ^{20}Ne. The same code (but without parity projection) was recently used to explore exotic shapes in proton-rich $N \simeq Z$ nuclei in the ^{80}Zr region [39, 40], and tetrahedral and triangular shapes are suggested to appear near the ground states of some nuclei in this region. In Refs. [34, 39, 40], the pairing correlations were taken into account in the BCS approximation. In the present calculation, we neglect the

pairing, since they are not expected to play an important role at high-spin states in ^{32}S.

When we allow for the simultaneous breaking of both reflection and axial symmetries, it is crucial to accurately fulfill the center-of-mass condition

$$< \sum_{i=1}^{A} x_i >=< \sum_{i=1}^{A} y_i >=< \sum_{i=1}^{A} z_i >= 0, \tag{2}$$

and the principal-axis condition

$$< \sum_{i=1}^{A} x_i y_i >=< \sum_{i=1}^{A} y_i z_i >=< \sum_{i=1}^{A} z_i x_i >= 0. \tag{3}$$

For this purpose we examined several techniques [41] and confirmed that the constrained HF procedure with quadrupole constraints [42] works well. Thus, we replace the "Routhian" $R = H - \omega_{\rm rot} J_x$ in eq. (1) with

$$R' = R - \sum_{k=1}^{3} \mu_k < \sum_{i=1}^{A} (x_k)_i >^2 - \sum_{k<k'}^{3} \mu_{k,k'} < \sum_{i=1}^{A} (x_k x_{k'})_i >^2 . \tag{4}$$

In numerical calculations, we confirmed that the constraints (2) and (3) are fulfilled to the order $O(10^{-15})$ with values of the parameters $\mu_k \sim O(10^2)$ and $\mu_{k,k'} \sim O(1)$. We solved these equations inside the sphere with radius R=8 [fm] and mesh size h=1 [fm], starting with various initial configurations. The 11-point formula was used as the difference formula for the Laplacian operator. As usual, the angular momentum is evaluated as $I\hbar =< J_x >$.

In this paper, we use the standard SIII and SkM* forces. With the use of the SIII force [26], Tajima et al. [30] carried out a systematic SHF+BCS calculation for the ground-state quadrupole deformations of nuclei in a wide area of nuclear chart. They have carefully examined the possible error due to the use of the mesh size h=1[fm] and found that the deformation energies obtained with this mesh size are quite accurate. On the other hand, the SkM* force [27] was designed to accurately describe properties at large deformations like fission barriers, so that it may be suited for the description of superdeformations [32]. In recent years, several newer versions of the Skyrme forces have been proposed (see, e.g. Ref. [43]) in order to improve isospin properties of the Skyrme forces. Although the major purpose of them is to better describing neutron-rich unstable nuclei, it will also be interesting to employ such versions to examine the dependence of the results reported in this paper on the effective interactions adopted. We defer such a more extensive calculation for the future.

3 Structure of the yrast line

The calculated yrast line is displayed in Fig. 1, and angular momenta and deformations of the yrast states are drawn as functions of rotational frequency in Figs. 2 and 3. In these and succeeding figures, the calculation were done in

step of $\Delta\omega_{\rm rot} = 0.2$ MeV/$\hbar$, and the calculated points (indicated by symbols) are smoothly interpolated by lines. The quadrupole deformation parameters β_2 and γ are defined as

$$\beta_2 \cos\gamma = \frac{4\pi}{5} < \sum_{i=1}^{A} r_i^2 Y_{20}(\theta_i, \phi_i) > / < \sum_{i=1}^{A} \boldsymbol{r}_i^2 >, \tag{5}$$

$$\beta_2 \sin\gamma = -\frac{4\pi}{5} < \frac{1}{\sqrt{2}} \sum_{i=1}^{A} r_i^2 (Y_{22}(\theta_i, \phi_i) + Y_{22}^*(\theta_i, \phi_i)) > / < \sum_{i=1}^{A} \boldsymbol{r}_i^2 > . \tag{6}$$

It is seen from Figs. 1-3 that the results of calculation with the SIII and SkM* forces are quite similar: For both cases, the expected SD band becomes the yrast for $I \geq 14$, and it exhibits a singular behavior at about $I \simeq 24$. As we shall discuss in the next section, this is due to a band crossing associated with the rotation-aligned $[440]\frac{1}{2}$ level, and we call the yrast states above $I \simeq 24$ "hyperdeformed (HD)-like configuration" in order to distinguish them from the SD configuration. This configuration becomes unstable against fission for $I \geq 34$. In addition to the SD and HD-like configurations mentioned above, we found that the yrast states with $5 \leq I \leq 13$ possess an appreciable amount of non-axial octupole deformation of the Y_{31} type, so that we call, for convenience, this region of the yrast line "Y_{31} band", although, as discussed in Section 7, some cautions are necessary in using this terminology.

Thus, the calculated yrast line can be roughly divided into the following four regions:
1) $I \leq 4$, weakly prolate region,
2) $5 \leq I \leq 13$, Y_{31} deformed region,
3) $14 \leq I \leq 24$, SD region,
4) $26 \leq I \leq 32$, HD-like region.

Below we first discuss the properties of the high-spin limit of the SD band, and later about the Y_{31} band. The lowest-spin region will be touched upon in Section 7 briefly.

4 High-spin limit of the SD band

As we saw in Figs. 1-3, the solutions of the cranked SHF equations corresponding to the yrast SD configuration are obtained from $I = 0$ to about $I = 22$.

Figure 4 shows the potential energy function for the SD state at $I = 0$, evaluated by means of the constrained HF procedure [42] with the quadratic constraint on the mass-quadrupole moment. We see that the excitation energy of the SD state at $I = 0$ is about 12 MeV.

A particularly interesting point is the behavior of the SD band in the high-spin limit: It is clearly seen in Figs. 2 and 3 that a jump occurs both in the angular momentum I and the quadrupole deformation β_2 at $\omega_{\rm rot} \simeq 2.9$

MeV/$\hbar$. At this point, I jumps from about 22 to 26, and β_2 suddenly increases from about 0.6 to 0.7. Such a discontinuity is well known [44] to occur in the description of the band crossing phenomena within a standard framework of the cranked mean-field approach. The point is more clearly seen in Fig. 5 as a singular behavior of the dynamical moment of inertia $\mathcal{J}^{(2)} = dI/d\omega_{\rm rot}$ near the band crossing point. (Other properties of $\mathcal{J}^{(2)}$ will be discussed in the next section.)

Figure 6 displays the shape evolution of the SD band as a function of angular momentum in the (β_2, γ) plane: With increasing angular momentum, small triaxial deformations gradually set in and at $I \simeq 24$ the shape exhibits a striking "back-bending" toward larger prolate deformations. Evidently, this is due to the band crossing mentioned above. Such a singular behavior of the SD band can be noticed also in the previous cranked HF calculation with the BKN force [18]. In Fig. 6 we also plot the I =24 and 26 states, which are missing in Figs. 1-3, by smoothly extrapolating the $I - \omega_{\rm rot}$ and $(\beta_2, \gamma) - I$ curves for the SD and the HD-like configurations, respectively (see, Ref. [44] for the treatment of the band-crossing region).

The microscopic origin of this singular behavior may be understood when we examine the single-particle energy diagram in the rotating frame (routhians) presented in Fig. 7. We see that the rotation-aligned level associated with the $[440]\frac{1}{2}$ orbit comes down in energy with increasing $\omega_{\rm rot}$ and crosses the Fermi level at $\omega_{\rm rot} \simeq 2.9$ MeV$\hbar$ which corresponds to $I \simeq 24$. Thus, the yrast states above $I \simeq 24$ are characterized by the occupation of the $[440]\frac{1}{2}$ level by a single proton and a neutron. According to the deformed harmonic-oscillator model, N=Z=18 is a magic number associated with the HD shell structure with axis ratio 3:1, in which the $[440]\frac{1}{2}$ level is occupied by two protons and two neutrons. In order to distinguish the yrast states with $I \geq 26$ from the SD states below $I \simeq 24$ and keeping in mind a connection to the HD configuration, we call them "the HD-like configuration", although the magnitude of the quadrupole deformation β_2 obtained in the SHF calculation is in fact comparable to that of the SD shape rather than the HD shape.

Let us note that if we regard the SD configuration as to correspond to the j-j-coupling shell model $4p$-$12h$ configuration $\pi[(f_{7/2})^2(sd)^{-6}] \otimes \nu[(f_{7/2})^2(sd)^{-6}]$ (relative to ^{40}Ca) in the spherical limit, the maximum angular momentum that can be generated by aligning the single-particle angular momenta toward the direction of the rotation axis is $24\hbar$, and thus "the SD band termination" might be expected at this angular momentum. Interestingly, our calculation indicates that a crossover to the HD-like configuration takes place just at this region of the yrast line.

5 Comparison with the CHO model

The behavior at the high-spin limit of the SD band obtained in the SHF calculation possesses some similarities with that expected from the CHO model.

This model has been frequently used [45–50] as a simplified model of rotating mean fields. With obvious notations, the single-particle Hamiltonian of this model is written as

$$h' = \sum_{k=1}^{3} \hbar\omega_k (c_k^\dagger c_k + \frac{1}{2}) - \omega_{\rm rot} l_1, \tag{7}$$

where

$$c_k^\dagger = \sqrt{m\omega_k/2\hbar}(x_k - ip_k/m\omega_k), \tag{8}$$

with (x_1, x_2, x_3) indicating (x, y, z), etc.

The orbital angular momentum operator l_1 consists of two parts:

$$l_1 = l_1^{(\Delta N=0)} + l_1^{(\Delta N=2)} \tag{9}$$

with

$$l_1^{(\Delta N=0)} = i\hbar \frac{\omega_2 + \omega_3}{2\sqrt{\omega_2\omega_3}}(c_3^\dagger c_2 - c_2^\dagger c_3), \tag{10}$$

$$l_1^{(\Delta N=2)} = i\hbar \frac{\omega_3 - \omega_2}{2\sqrt{\omega_2\omega_3}}(c_2^\dagger c_3^\dagger - c_3 c_2). \tag{11}$$

For a given value of $\omega_{\rm rot}$ or $I\hbar =< \sum_{i=1}^{A}(l_1)_i >$, one can determine the oscillator frequencies $(\omega_1, \omega_2, \omega_3)$ such that the selfconsistency condition between the density and the potential,

$$\omega_1^2 < \sum_{i=1}^{A}(x_1^2)_i >= \omega_2^2 < \sum_{i=1}^{A}(x_2^2)_i >= \omega_3^2 < \sum_{i=1}^{A}(x_3^2)_i >, \tag{12}$$

is fulfilled under a volume conservation condition [50]. Here, the brackets denote expectation values with respect to Slater determinantal states composed of single-particle eigenmodes of h'.

Let us denote the total number of quanta in each of the three directions $(k = 1, 2, 3)$ at $\omega_{\rm rot} = 0$ as

$$\Sigma_k =< \sum_{i=1}^{A}(c_k^\dagger c_k + \frac{1}{2})_i >, \tag{13}$$

and let us continuously follow the configuration specified by the set of values $(\Sigma_1, \Sigma_2, \Sigma_3)$ which are defined at $\omega_{\rm rot} \neq 0$ as the number of quanta associated with the normal modes of the CHO Hamiltonian h'. In terms of Σ_k, the selfconsistency condition at $\omega_{\rm rot} = 0$ is written as

$$\omega_1\Sigma_1 = \omega_2\Sigma_2 = \omega_3\Sigma_3. \tag{14}$$

If the $\Delta N = 2$ part of the angular momentum operator l_1 is neglected, it is well known that there exists a maximum angular momentum $I_c = \Sigma_3 - \Sigma_2$ for a given configuration $(\Sigma_1, \Sigma_2, \Sigma_3)$, where the shape is oblate and the symmetry axis coincides with the rotation axis [45]. This shape evolution is caused by

the effect of the $\Delta N = 0$ part of the cranking term, which tends to align the angular momentum of individual particles toward the rotation axis of the system (rotation alignment effect due to the Coriolis force). In the case of the doubly closed shell configuration for the SD magic number $N = Z = 16$ (including the spin-degeneracy factor 2), corresponding to the SD band in ^{32}S, $(\Sigma_1, \Sigma_2, \Sigma_3) = (24, 24, 48)$ taking into account protons and neutrons. We would thus expect the "SD band termination" at the maximum angular momentum $I_c = \Sigma_3 - \Sigma_2 = 24$. This number coincides with that evaluated in the previous section in relation to the j-j coupling shell-model configurations.

On the other hand, the $\Delta N = 2$ part stretches the system toward larger deformations, and actual shape evolutions as functions of angular momentum are determined by the competition and balance between these two effects. Fully taking into account both effects of the cranking term, Troudet and Arvieu [49, 50] found that there is a critical value α_c of Σ_3/Σ_2,

$$\alpha_c = \frac{\sqrt{27} + \sqrt{2}}{\sqrt{27} - \sqrt{2}} \simeq 1.75, \tag{15}$$

such that the configuration $(\Sigma_1, \Sigma_2, \Sigma_3)$ does not (does) reach the oblate limit if Σ_3/Σ_2 is greater (less) than α_c. This is because, for large deformations, the stretching effect of the $\Delta N = 2$ term dominates at high spin over the alignment effect of the $\Delta N = 0$ term. In the case of ^{32}S, the SD configuration have $\Sigma_3/\Sigma_2 = \omega_2/\omega_3 = 2 > \alpha_c$ at $I = 0$. Therefore, the "oblate limit" mentioned above will not be reached and the shape at the "band termination" point will be triaxial.

Figure 8 shows the shape evolution in the (β_2, γ) plane, calculated for the SD configuration of ^{32}S in the CHO model. Here, the result of calculation for the configuration (22,24,54) is also presented, as an example of the HD-like configurations. We see that, although the triaxiality slowly sets in with increasing angular momentum, the shape of the SD states remains rather far from the oblate limit and exhibits a striking "back-bending" at about $I_c = 24$ toward larger prolate deformations for $I \geq I_c$. Apparently, the behavior near the critical angular momentum I_c for the SD band is quite similar to that of the SHF solutions presented in the previous section. On the other hand, it should be recalled in comparing Fig. 8 with Fig. 6 that the highest spin region of $I = 26 \sim 32$ on the yrast line corresponds to the HD-like configuration in the SHF solution: While the continuation of the SD configuration (24,24,48) to the $I > 24$ region as well as that of the HD-like configuration (22,24,54) to the $I < 26$ region are presented for the CHO model, only the yrast states were obtained and plotted in the SHF calculation.

Figure 9 shows the angular momentum and the dynamical moment of inertia $\mathcal{J}^{(2)}$ as functions of the rotational frequency. We see that $\mathcal{J}^{(2)}$ gradually decreases until the critical point. It is interesting to compare this property with that of $\mathcal{J}^{(2)}$ for the SD band in the SHF calculation (Fig. 5). Apparently, they are quite similar. This suggests that the gradual decrease with increasing $\omega_{\rm rot}$ of the dynamical moment of inertia for the SD band is rooted in the

existence of the critical angular momentum I_c associated with the quantum SD shell structure. We feel that a more detailed investigation of the SD states near the "band termination" point is a very important and challenging subject for a deeper understanding of the rotational motion of the nucleus as a finite Fermion system,

6 Effects of time-odd components

In this section we shortly discuss about the rotation-induced, time-odd components in the mean field. The moment of inertia of the SD band is expected to be a good physical quantity for identifying the effects of the time-odd components, since the pairing correlation plays only a minor role there. Concerning the effect of various time-odd components on the moment of inertia, we refer some recent works; [51] for a semiclassical description, [52] for a rotating nuclear matter, and [53] for SD bands around ^{152}Dy.

Table 1 shows individual contributions from various kinds of time-odd term. It is interesting to note that the contributions from terms containing the spin-density, $\boldsymbol{\rho}(\boldsymbol{r})$, nearly cancel out with each other and, accordingly, the contribution from the current-density terms, denoted by $B_3 + B_4$, dominates in the sum. Such a remarkable cancellation of the spin-density terms was not seen in the case of ^{152}Dy [53], and may be specific to ^{32}S under consideration.

In Fig. 10 we compare the results of calculation with and without the time-odd components. It is seen that the time-odd components increase the angular momentum for a given value of $\omega_{\rm rot}$. Accordingly, the dynamical moment of inertia $\mathcal{J}^{(2)} = dI/d\omega_{\rm rot}$ also increases. This trend is understood from the consideration of the local Galilean invariance of the Skyrme force [51, 53] (for a more general analysis not restricted to the Skyrme force, see [45, 52]): If the time-odd components is neglected, the local Galilean invariance is violated and we obtain the moment of inertia associated with the effective mass m^*. By including the time-odd components, however, the local Galilean invariance is restored and we get the moment of inertia associated with the nucleon mass m. The calculated result presented in Fig. 10 is consistent with this expectation, but a more quantitative analysis is not necessarily easy, because, as seen in Fig. 5, the calculated moment of inertia significantly deviates from the rigid-body value due to the shell effect.

Table 1
Contributions from various terms in the time-odd energy density,

$$H_{\rm odd}(\boldsymbol{r}) = -B_3\boldsymbol{j}^2 - B_4(\boldsymbol{j}_n^2+\boldsymbol{j}_p^2) + B_9(\boldsymbol{j}\cdot\nabla\times\boldsymbol{\rho}+\boldsymbol{j}_n\cdot\nabla\times\boldsymbol{\rho}_n+\boldsymbol{j}_p\cdot\nabla\times\boldsymbol{\rho}_p) \\ +B_{10}\boldsymbol{\rho}^2 + B_{11}(\boldsymbol{\rho}_n^2+\boldsymbol{\rho}_p^2) + B_{12}\rho^\alpha\boldsymbol{\rho}^2 + B_{13}\rho^\alpha(\boldsymbol{\rho}_n^2+\boldsymbol{\rho}_p^2),$$

to the energy (in MeV), calculated at $\omega_{\rm rot} = 1.0$ MeV/$\hbar$ for the SIII and SkM* forces. Here, $(\boldsymbol{j}_n, \boldsymbol{j}_p)$ and $(\boldsymbol{\rho}_n, \boldsymbol{\rho}_p)$ denote the nucleon currents and the spin densities (for neutrons and protons), respectively, and $\boldsymbol{j} = \boldsymbol{j}_n + \boldsymbol{j}_p$ and $\boldsymbol{\rho} = \boldsymbol{\rho}_n + \boldsymbol{\rho}_p$ (see Ref. [34] for their explicit expressions). In columns designated by coefficients B_i, values after the spatial integration are listed. while the total value $\int d\boldsymbol{r} H_{\rm odd}(\boldsymbol{r})$ and the sum of contributions from the current terms (the first two terms in the r.h.s. of the above equation) are shown in the columns denoted by "total" and "$B_3 + B_4$", respectively. For reference, the effective mass m^* in nuclear matter for each force is also listed.

	B_3	B_4	B_9	B_{10}	B_{11}	B_{12}	B_{13}	total	B_3+B_4	m^*/m
SIII	-1.94	0.79	-0.17	-0.77	0.86	0.37	-0.18	-1.04	-1.15	0.76
SkM*	-1.83	0.90	-0.38	-0.44	2.45	0.00	-1.65	-0.95	-0.93	0.79

7 Y_{31} deformation

As mentioned in Section 3, we found that the yrast states in the region $5 \leq I \leq 13$ possess a significant amount of non-axial octupole deformations of the Y_{31} type. It should be emphasized that such an exotic deformation is absent at $I = 0$ but emerges at high spin. It has become possible to get this kind of solution by using the new cranked SHF code allowing for the simultaneous breaking of both axial and reflection symmetries.

As in [39], we define the octupole deformation parameters α_{3m} as

$$\alpha_{3m} = (4\pi/3AR^3) < \sum_{i=1}^{A}(r^3 X_{3m})_i >, \qquad (m = -3, \cdots, 3) \tag{16}$$

with $R = 1.2A^{1/3}$ fm. Here X_{3m} is a real basis of the spherical harmonics,

$$X_{30} = Y_{30}, \qquad X_{3|m|} = \frac{1}{\sqrt{2}}(Y_{3-|m|} + Y^*_{3-|m|}), \\ X_{3-|m|} = \frac{-i}{\sqrt{2}}(Y_{3|m|} - Y^*_{3|m|}), \tag{17}$$

where the quantization axis is chosen as the largest and smallest principal inertia axes for prolate and oblate solutions, respectively. The yrast solutions

in the region $5 \leq I \leq 13$ have $\alpha_{31} \neq 0$ but $\alpha_{3m} = 0$ for $m \neq 1$. (See [54] for a general discussion on this kind of deformation and its consequence on rotational spectra.) Figure 11 shows the calculated values of the Y_{31} deformation as a function of $\omega_{\rm rot}$. We see that the α_{31} value quickly rises when $\omega_{\rm rot}$ exceeds 1 MeV/$\hbar$.

The microscopic origin of the growth of the non-axial octupole deformation α_{31} may be understood when we examine the single-particle energy diagram in the rotating frame (routhians) presented in Fig. 12. We note that a strong coupling and a quasi-level crossing between the rotation-aligned $[330]\frac{1}{2}$ orbit and the $[211]\frac{1}{2}$ orbit take place near the Fermi surface in the region $1.0 \leq \omega_{\rm rot} \leq 2.2$ MeV/$\hbar$. The matrix element of the $r^3 Y_{31}$ operator between the two single-particle states is large, since they satisfy the selection rule for the asymptotic quantum numbers ($\Delta\Lambda = 1, \Delta n_z = 2$). This strong coupling is responsible for the α_{31} deformation appearing in this region of the yrast line.

Figure 13 shows the potential energy function with respect to the α_{31} direction, calculated by means of the constrained HF procedure. Note the scale of the ordinate. Although we obtain a clear minimum at a finite value of α_{31}, the potential is rather shallow in this direction, so that the amplitude of the quantum-mechanical zero-point vibrational motion might be larger than the equilibrium deformation. If this is the case, a treatment of dynamics going beyond the mean-field approximation is required in order to investigate the consequence of the α_{31} deformation on the quantum spectra in the yrast region under consideration. This is beyond the scope of the present paper.

It may be desirable to extend the potential energy curve in Fig. 13 to the $\alpha_{31} = 0$ limit. It turned out, however, difficult to do so, because many level-crossings take place with decreasing α_{31}. [If we extrapolate to this limit assuming parabolic dependence on α_{31}, we obtain about 2 MeV as a very crude estimate of the energy gain due to the α_{31} deformation.] By the same reason, it is also difficult to follow the continuation of the Y_{31} band to the higher spin region as soon as it departs from the yrast line.

8 Some remarks on experimental data

Although rich experimental data are available for excited states of ^{32}S, the high-spin yrast region in which we are interested is rather poorly known at the present time. Accordingly, we discuss experimental references only briefly.

For low-spin states with $I \leq 7$, detailed spectroscopic data are available up to excitation energy 11.76 MeV [19, 20]. These excited states are shown to be well described by the spherical shell model calculations [19,20]. In these works, some negative-parity states were interpreted as octupole-quadrupole phonon multiplets. As a matter of fact, we need to go beyond the simple mean field theory in order to discuss such spectroscopic data in the low-spin region.

Highly excited states have been studied by various nuclear reactions as well as ^{16}O-^{16}O scatterings. Investigating the ^{16}O(^{20}Ne, α)^{32}S(α)^{28}Si (g.s.)

reaction, Morita et al [55] suggested possible band structures of the quasi-molecular configuration of ^{16}O+^{16}O and of some parity-doublet-like structures with angular momenta $5^-, 6^+, (7^-), (8^+)$ at the 12-15 MeV region. Recently, Curtis et al [56] investigated the region with I=10-16 and the excitation energy 32-38 MeV by means of the ^{12}C(^{24}Mg,^{16}O^{16}O)^{4}He reaction, and suggested an existence of highly deformed states in this region. It is tempting to compare these experimental data with our theoretical calculations. The experimentally explored regions are, however, about 10 MeV above the theoretical yrast line. Therefore, a more detailed spectroscopic study is needed in order to associate these data with the yrast structure.

9 Conclusions

We have investigated the high-spin yrast structure of ^{32}S by means of the cranked SHF method in the 3D Cartesian-mesh representation without imposing restrictions on spatial symmetries, and suggested that
1) a crossover from the SD to the HD-like configurations takes place on the yrast line at angular momentum $I \simeq 24$, which corresponds to the "band termination" point in the CHO model, and
2) non-axial octupole deformations of the Y_{31} type play an important role in the yrast states in the range $5 \leq I \leq 13$.

In conclusion, we would like to stress again that the calculated yrast line for I= 14-20 lies about 10 MeV below the observed molecular resonance region associated with the ^{16}O-^{16}O configurations. Thus, a yrast γ-spectroscopy with higher resolving power is strongly desired in order to explore the high-spin region of the yrast line of ^{32}S .

Acknowledgements

During the course of this work, we have benefited from discussions with J. Dobaczewski, P.-H. Heenen, M. Matsuo, W. Nazarewicz, N. Tajima, S. Takami and K. Yabana. We would like to express our hearty thanks to them. We are grateful to S. Frauendorf for pointing out the importance of distinguishing the α_{31} and the α_{3-1} deformations and sending us his article [54] before publication. This work was supported by the Grant-in-Aid for Scientific Research (No. 10640264) from the Japan Society for the Promotion of Science.

References

[1] P.J. Nolan and P.J. Twin, Annu. Rev. Nucl. Part. Sci. 38 (1988) 533.

[2] S. Åberg, H. Flocard and W. Nazarewicz, Annu. Rev. Nucl. Part. Sci. 40 (1990) 439.

[3] R.V.F. Janssens and T.L. Khoo, Annu. Rev. Nucl. Part. Sci. 41 (1991) 321.

[4] C. Baktash, B. Haas and W. Nazaerewicz, Annu. Rev. Nucl. Part. Sci. 45 (1995) 485.

[5] C. Baktash, Prog. Part. Nucl. Phys. 38 (1997) 291.

[6] J. Dobaczewski, Proc. Int. Conf. on Nuclear Structure '98, Gatlinburg, Tennessee, August 10-15, 1998, ed. C. Baktash, in press; nucl-th/9811043.

[7] R.K. Sheline, I. Ragnarsson and S.G. Nilsson, Phys. Lett. B 41 (1972) 115.

[8] G. Leander and S.E. Larsson, Nucl. Phys. A 239 (1975) 93.

[9] I. Ragnarsson, S.G. Nilsson and R.K. Sheline, Phys. Rep. 45 (1978) 1.

[10] T. Bengtsson, M.E. Faber, G. Leander, P. Möller, M. Ploszajczak, I Ragnarsson and S. Åberg, Phys. Scr. 24 (1981) 200.

[11] Y. Abe, Y. Kondo and T. Matsuse, Prog. Theor. Phys. Supple. 68 (1980) 303.

[12] W. Greiner, J. Y. Park and W. Scheid, Nuclear Molecule (World Scientific, Singapore, 1995).

[13] W. Nazarewicz and J. Dobaczewski, Phys. Rev. Lett. 68 (1992) 154.

[14] M. Freer, R.R. Betts and A.H. Wuosmaa, Nucl. Phys. A 587 (1995) 36.

[15] M. Freer and A.C. Merchant, J. Phys. G 23 (1997) 261, and references therein.

[16] Y. Fujiwara, H. Horiuchi, K. Ikeda, M. Kamimura, K. Katō, Y. Suzuki and E. Uegaki, Prog. Theor. Phys. Supple. 68 (1980) 29.

[17] M. Girod and B. Grammaticos, Phys. Rev. C 27 (1983) 2317.

[18] H. Flocard, P.H. Heenen, S.J. Krieger and M.S. Weiss, Prog. Theor. Phys. 72 (1984) 1000.

[19] J. Brenneison et al, Z. Phys. A 357 (1997) 157; *ibid* A 357 (1997) 377

[20] A. Kangasmäki et al, Phys. Rev. C 58 (1998) 699.

[21] P.G. Zint and U. Mosel, Phys. Lett. B 58 (1975) 269.

[22] W. Bauhoff, H. Schultheis and R. Schultheis, Phys. Rev. C 22 (1980) 861.

[23] H. Schultheis and R. Schultheis, Phys. Rev. C 25 (1982) 2126.

[24] J. Zhang, W.D.M. Rae and A.C. Merchant, Nucl. Phys. A 575 (1994) 61.

[25] J. Cseh, G. Lévai, A. Ventura, L. Zuffi, Phys. Rev. C 58 (1998) 2144.

[26] M. Beiner, H. Flocard, Nguyen van Giai and P. Quentin, Nucl. Phys. A 238 (1975) 29.

[27] J. Bartel, P. Quentin, M. Brack, C. Guet and H.-B. Håkansson, Nucl. Phys. A 386 (1982) 79.

[28] K.T.R. Davies, H. Flocard, S.J. Krieger and M.S. Weiss, Nucl. Phys. A 342 (1980) 111.

[29] P. Bonche, H. Flocard, P.H. Heenen, S.J. Krieger and M.S. Weiss, Nucl. Phys. A 443 (1985) 39.

[30] N. Tajima, S. Takahara and N. Onishi, Nucl. Phys. A 603 (1996) 23.

[31] P. Bonche, S. Koonin and J.W. Negele, Phys. Rev. C 13 (1976) 1226.

[32] S. Takahara, N. Tajima and N. Onishi, Nucl. Phys. A 642 (1998) 461.

[33] H. Flocard, P.H. Heenen, S.J. Krieger and M.S. Weiss, Nucl. Phys. A 391 (1982) 285.

[34] P. Bonche, H. Flocard, P.H. Heenen, Nucl. Phys. A 467 (1987) 115.

[35] M. Yamagami and K. Matsuyanagi, Proc. Int. Conf. on Nuclear Structure '98, Gatlinburg, Tennessee, August 10-15, 1998, ed. C. Baktash, in press; nucl-th/9809038.

[36] H. Molique, J. Dobaczewski and J. Dudek, Preprint nucl-th/9907103.

[37] E. Chabanat, P. Bonche, P. Haensel, J. Meyer and F. Schaeffer, Nucl. Phys. A 635 (1998) 231.

[38] S. Takami, K. Yabana and K. Ikeda, Prog. Theor. Phys. 96 (1996) 407.

[39] S. Takami, K. Yabana and M. Matsuo, Phys. Lett. B 431 (1998) 242.

[40] M. Matsuo, S. Takami and K. Yabana, Proc. Int. Conf. on Nuclear Structure '98, Gatlinburg, Tennessee, August 10-15, 1998, ed. C. Baktash, in press; Preprint YITP-98-69.

[41] M. Yamagami, Master thesis (Kyoto University, 1997).

[42] H. Flocard, P. Quentin, A.K. Kerman and D. Vautherin, Nucl. Phys. A 203 (1973) 433.

[43] P.-G. Reinhard, D.J.Dean, W. Nazarewicz, J. Dobaczewski, J.A. Maruhn and M.R. Strayer, Phys. Rev. C 60 (1999) 014316.

[44] I. Hamamoto, Treatise on Heavy-Ion Science, Vol. 3, ed. D.A. Bromley (Plenum, New York, 1985) p.313.

[45] A. Bohr and B.R. Mottelson, Nuclear Structure, Vol. 2 (Benjamin, Reading, MA, 1975).

[46] J. G. Valatin, Proc. Roy. Soc.(London), A 238 (1956) 132.

[47] G. Ripka, J. P. Blaizot and N. Kassis, Heavy Ions, High Spin States and Nuclear Structure (IAEA, Vienna, 1975) Vol. 1, p.445.

[48] V.G. Zelevinski, Sov. J. Nucl. Phys. 22 (1975) 565.

[49] T. Troudet and R. Arvieu, Z. Phys. A 291 (1979) 183.

[50] T. Troudet and R. Arvieu, Ann. Phys. 134 (1981) 1.

[51] K. Bencheikh, P. Quentin and J. Bartel, Nucl. Phys. A 571 (1994) 518.

[52] S. Frauendorf and K. Neergård, Z. Phys. A 354 (1996) 381.

[53] J. Dobaczewski and J. Dudek, Phys. Rev. C 52 (1995) 1827; *ibid* C 55(1997) 3177(E).

[54] S. Frauendorf, to be published in Rev. Mod. Phys.

[55] K. Morita et al, Phys. Rev. Lett. 55 (1985) 185.

[56] N. Curtis et al, Phys. Rev. C 53 (1996) 1804.

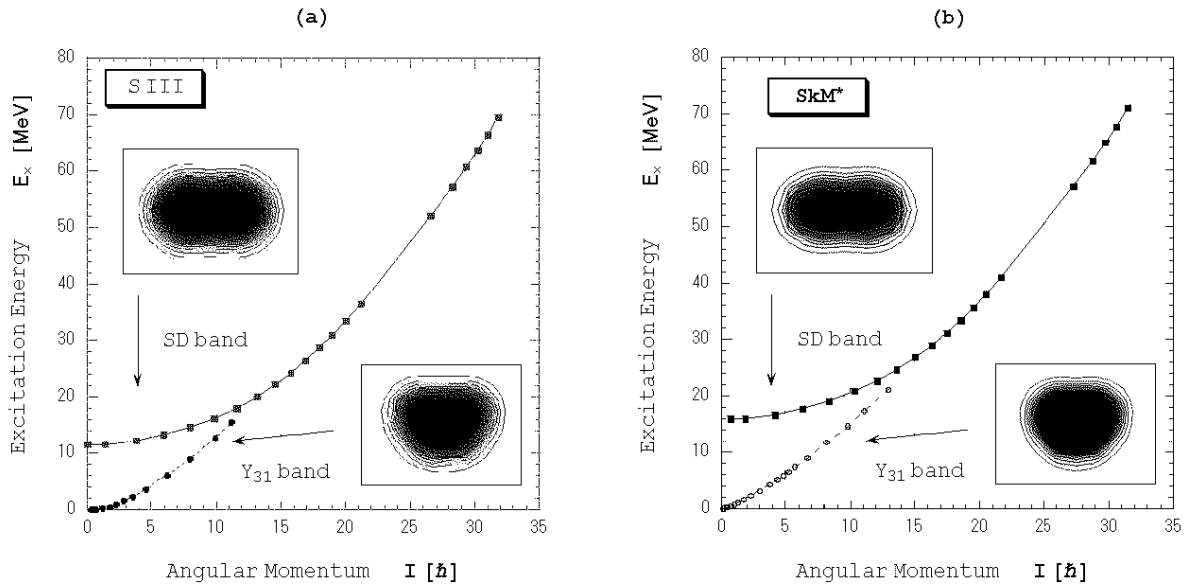

Figure 1: (a) Excitation energy vs. angular-momentum plot for the yrast structure of ^{32}S, calculated with the SIII force. Density distributions on the plane *perpendicular* to the rotation axis are shown, as insets, for the SD band (solid line) and the Y_{31} band (dashed line). The calculation was done in step of $\Delta\omega_{\rm rot} = 0.2$ MeV/$\hbar$, and the calculated points (indicated by symbols) are smoothly interpolated by lines. (b) Same as (a), but with the SkM* force.

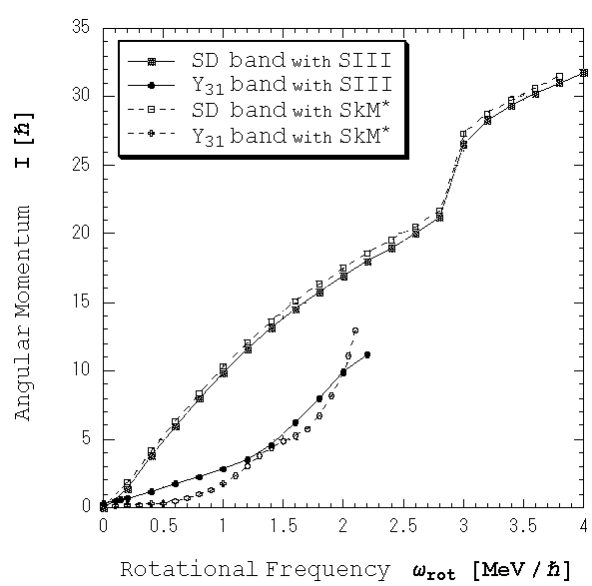

Figure 2: Angular momentum I plotted as a function of rotational frequency $\omega_{\rm rot}$ for the SD band and the Y_{31} band in ^{32}S. Results calculated with the SIII and SkM* forces are shown by solid and dashed lines, respectively.

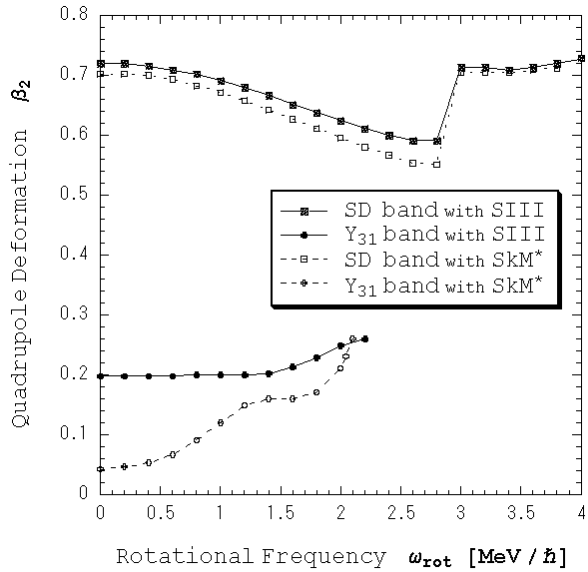

Figure 3: Quadrupole deformation β_2 plotted as a function of rotational frequency ω_{rot} for the SD band and the Y_{31} band in ^{32}S. Results calculated with the SIII and SkM* forces are shown by solid and dashed lines, respectively.

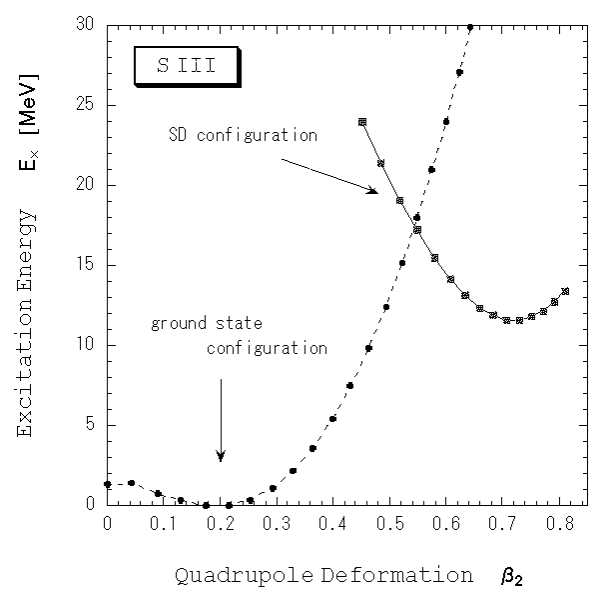

Figure 4: Potential energy function at $I = 0$ for the SD configuration (solid line) relative to that for the ground state configuration (dashed line) in ^{32}S, calculated with the SIII force.

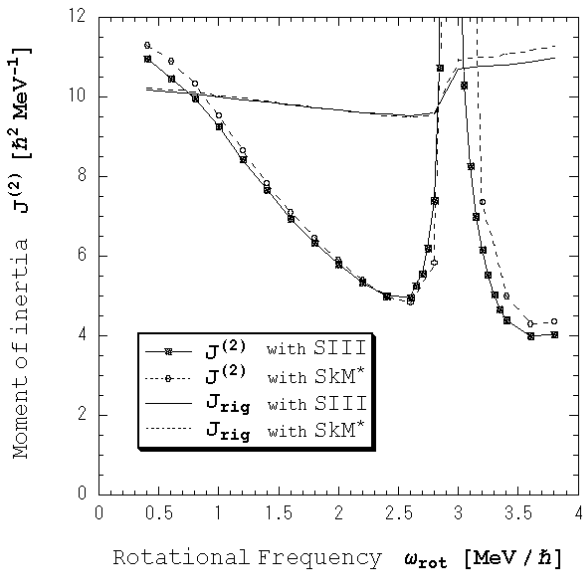

Figure 5: Dynamical moment of inertia $\mathcal{J}^{(2)} = dI/d\omega_{\rm rot}$ plotted as a function of $\omega_{\rm rot}$ for the SD band in ^{32}S. Results calculated with the SIII and SkM* forces are shown by solid and dashed lines, respectively. For reference, the rigid moments of inertia $\mathcal{J}_{\rm rig} = m \int \rho(\boldsymbol{r})(y^2+z^2)d\boldsymbol{r}$ with the calculated density $\rho(\boldsymbol{r})$ are also indicated.

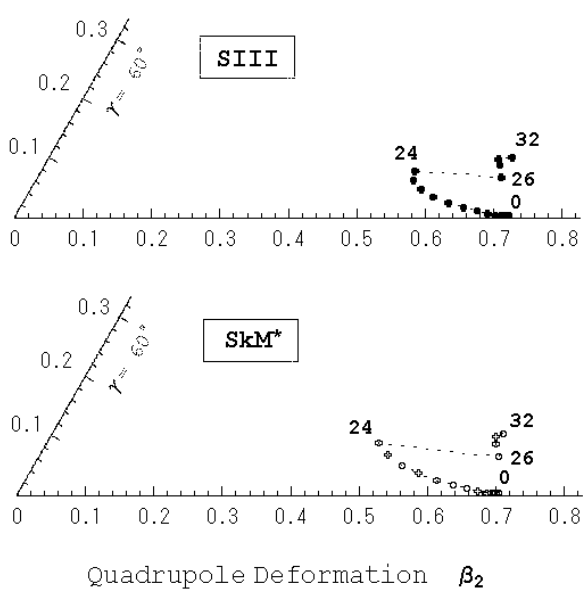

Figure 6: Shape evolution as a function of angular momentum, plotted in the (β_2, γ) plane for the SD and HD-like configurations in ^{32}S. Results calculated with the SIII and SkM* forces are separately shown.

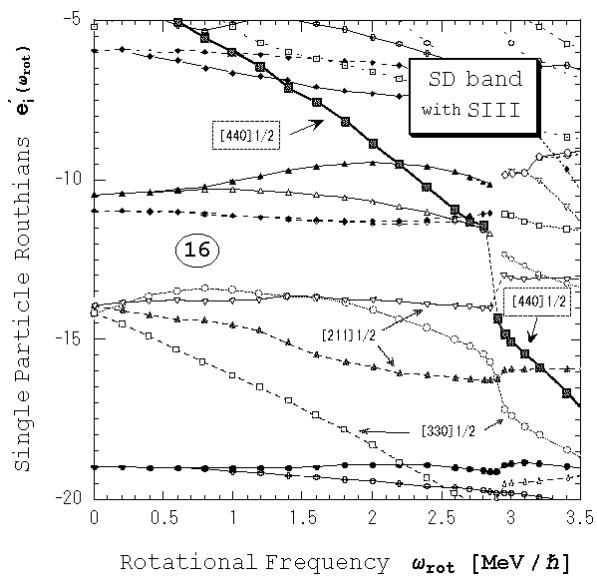

Figure 7: Single-particle energy diagram (for neutrons) in the rotating frame for the SD band in ^{32}S, plotted as a function of $\omega_{\rm rot}$. The SIII force is used. Note that the structure of the yrast configuration drastically changes at $\omega_{\rm rot} \simeq 2.9$ MeV/$\hbar$, so that the diagram is discontinuous about this point, although levels characterized by the same asymptotic quantum numbers are linked by lines.

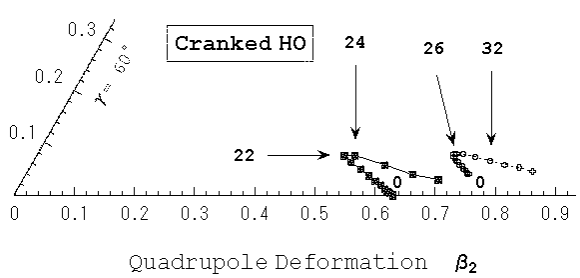

Figure 8: Shape evolutions as functions of angular momentum in the (β_2, γ) plane, plotted with filled and open symbols, respectively, for the SD configuration $(\Sigma_1, \Sigma_2, \Sigma_3) = (24, 24, 48)$ and the HD-like configuration (22,24,54) in the CHO model.

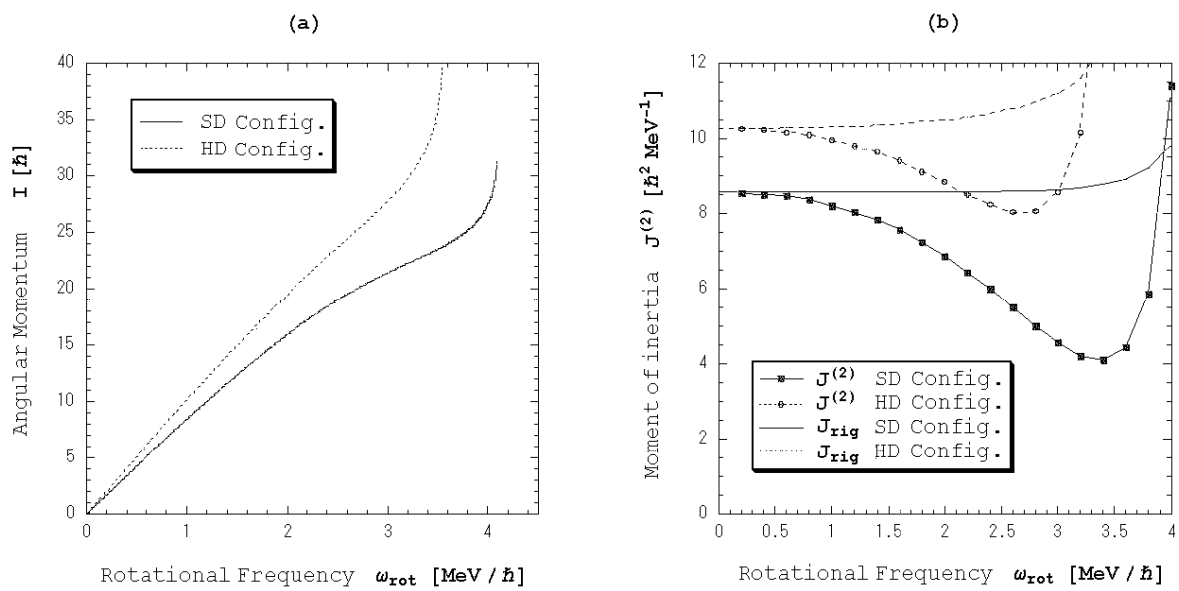

Figure 9: (a) Plot of angular momentum vs. rotational frequency in the CHO model. Solid line is used for the SD configuration $(\Sigma_1, \Sigma_2, \Sigma_3) = (24, 24, 48)$, while dashed line for the HD-like configuration (22,24,54). (b) Same as (a), but for dynamical moment of inertia $\mathcal{J}^{(2)} = dI/d\omega_{\rm rot}$. For reference, rigid moments of inertia $\mathcal{J}_{\rm rig} = m < \sum_{i=1}^{A}(y^2 + z^2)_i >$ for these configurations are also indicated.

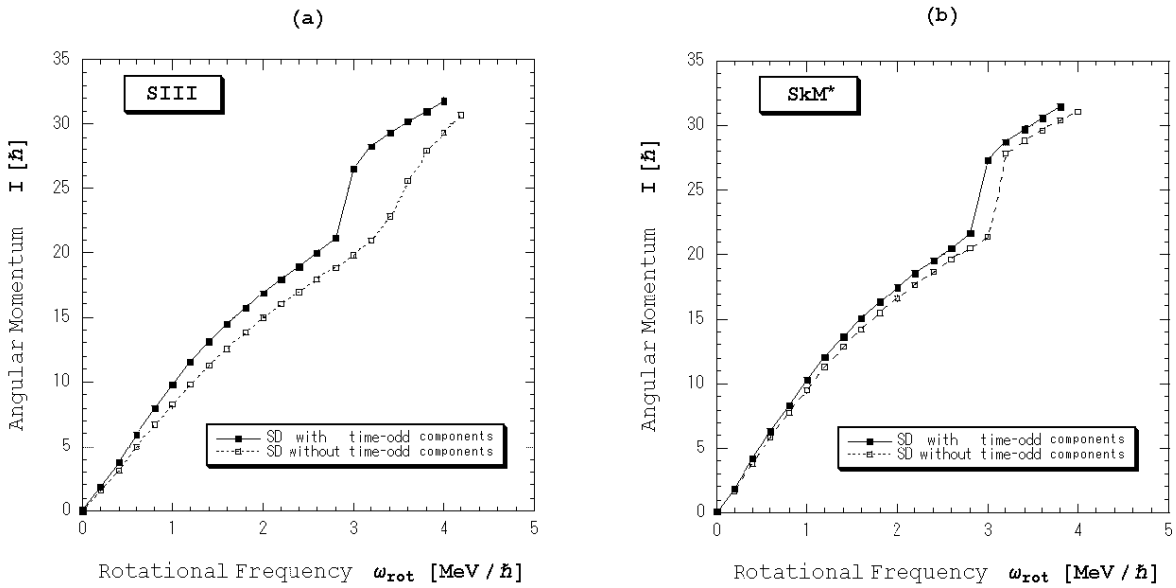

Figure 10: (a) Angular momentum I plotted as a function of $\omega_{\rm rot}$ for the SD band in ^{32}S. Solid line with filled squares (dashed line with open squares) indicates the result with(without) the time-odd components. The SIII force is used. (b) Same as (a), but with the SkM* force.

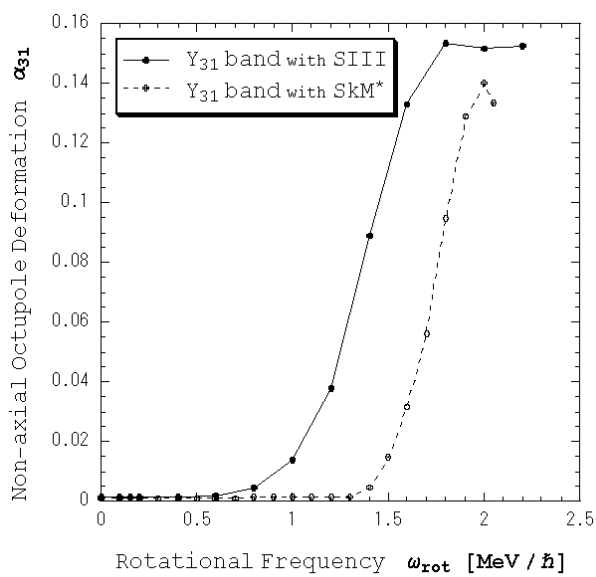

Figure 11: Non-axial octupole deformation α_{31} plotted as a function of $\omega_{\rm rot}$ for the Y_{31} band in ^{32}S. Results calculated with the SIII and SkM* forces are shown by solid and dashed lines, respectively.

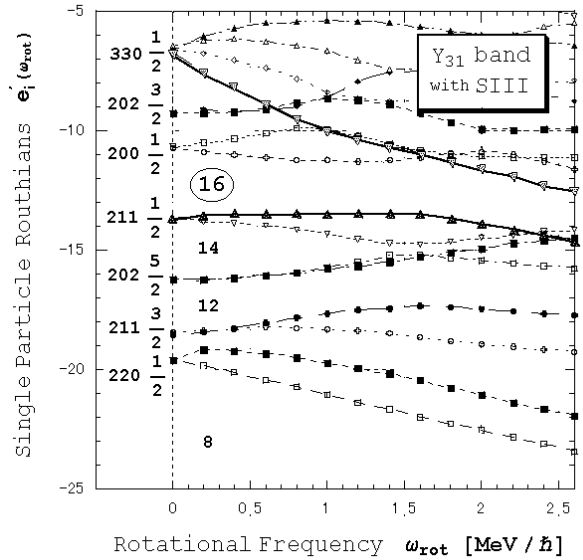

Figure 12: Single-particle energy diagram (for neutrons) in the rotating frame for the Y_{31} band in ^{32}S, plotted as a function of $\omega_{\rm rot}$. The SIII force is used.

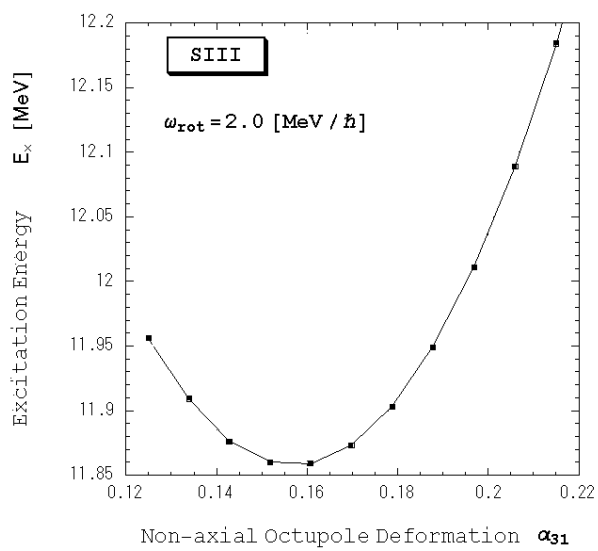

Figure 13: Potential energy function for the Y_{31} band in ^{32}S at $\omega_{\rm rot} = 2.0$ MeV/$\hbar$, calculated by means of the constrained HF procedure with the SIII force. Note the scale of the ordinate.